JACS
JOURNAL OF THE AMERICAN CHEMICAL SOCIETY
Article
pubs.acs.org/JACS

Fine Tuning the Performance of Multiorbital Radical Conductors by Substituent Effects

Aaron Mailman,[†] Joanne W. L. Wong,[†] Stephen M. Winter,[†] Robert C. M. Claridge,[†] Craig M. Robertson,[‡] Abdeljalil Assoud,[†] Wenjun Yong,[§] Eden Steven,[∥] Paul A. Dube,[⊥] John S. Tse,[#] Serge Desgreniers,[▽] Richard A. Secco,[§] and Richard T. Oakley*[,†]

[†]Department of Chemistry, University of Waterloo, Waterloo, Ontario N2L 3G1, Canada
[‡]Department of Chemistry, University of Liverpool, Liverpool L69 7ZD, United Kingdom
[§]Department of Earth Sciences, University of Western Ontario, London, Ontario N6A 5B7, Canada
[∥]Department of Physics, Florida State University, Tallahassee, Florida 32310, United States
[⊥]Brockhouse Institute for Materials Research, McMaster University, Hamilton, Ontario L8S 4M1, Canada
[#]Department of Physics, University of Saskatchewan, Saskatoon, Saskatchewan S7N 5E2, Canada
[▽]Department of Physics, University of Ottawa, Ottawa, Ontario K1N 6N5, Canada

Supporting Information

ABSTRACT: A critical feature of the electronic structure of oxobenzene-bridged bisdithiazolyl radicals **2** is the presence of a low-lying LUMO which, in the solid state, improves charge transport by providing additional degrees of freedom for electron transfer. The magnitude of this multiorbital effect can be fine-tuned by variations in the π-electron releasing/accepting nature of the basal ligand. Here we demonstrate that incorporation of a nitro group significantly stabilizes the LUMO, and hence lowers U_{eff}, the effective Coulombic barrier to charge transfer. The effect is echoed, at the molecular level, in the observed trend in E_{cell}, the electrochemical cell potential for **2** with R = F, H and NO_2. The crystal structures of the MeCN and EtCN solvates of **2** with R = NO_2 have been determined. In the EtCN solvate the radicals are dimerized, but in the MeCN solvate the radicals form superimposed and evenly spaced π-stacked arrays. This highly 1D material displays Pauli-like temperature independent paramagnetic behavior, with $\chi_{TIP} = 6 \times 10^{-4}$ emu mol^{-1}, but its charge transport behavior, with σ_{RT} near 0.04 S cm^{-1} and $E_{act} = 0.05$ eV, is more consistent with a Mott insulating ground state. High pressure crystallographic measurements confirm uniform compression of the π-stacked architecture with no phase change apparent up to 8 GPa. High pressure conductivity measurements indicate that the charge gap between the Mott insulator and metallic states can be closed near 6 GPa. These results are discussed in the light of DFT band structure calculations.

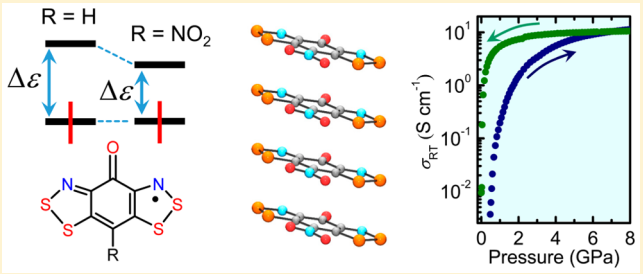

INTRODUCTION

The idea that the unpaired electron in an organic radical might serve as a carrier of charge, much like the valence electron in an elemental metal like sodium, goes back over a century,[1] but it was not until the mid-1970s that Robert Haddon proposed design criteria for a functional material based on the neutral radical conductor concept.[2] Recognizing the inherent weakness of intermolecular interactions between organic molecules in the solid state, Haddon concluded that charge transport required reduction of the potential energy barrier to charge transfer (U) to the point that the low kinetic energy of the unpaired electrons, expressed in terms of the hopping integral (t) between singly occupied molecular orbitals (SOMOs) on neighboring radicals, would be sufficient to allow charge migration. With respect to a hypothetical 1D-array of radicals, these ideas imply formation of a metallic state with a half-filled ($f = 1/2$) energy band when the bandwidth $W \sim 4|t| > U$.[3,4] However, for most organic π-radicals the reverse condition ($W < U$) applies, and they possess Mott insulating ground states.[5] Haddon's proposed solution, which has inspired and guided research on neutral radical conductors ever since, was to employ odd-alternant hydrocarbons based on the phenalenyl (PLY) framework, in which the highly delocalized, nonbonding SOMO promotes a low U-value. Following his lead the last 40 years has witnessed extensive research into the structures and properties of PLY derivatives,[6] including the exploration of substituent effects,[7] complex polycyclic systems,[8] mixed-valence spiro-conjugated PLYs,[9,10] and modes of association.[11] However, although materials constructed from a purely carbon-based framework displaying high conductivity have been generated,[12] metallic behavior has remained elusive.

Received: November 14, 2016
Published: January 24, 2017

DOI: 10.1021/jacs.6b11779
J. Am. Chem. Soc. 2017, 139, 1625−1635

An alternative approach to organic radical-based conductors involves the use of heavy heteroatoms.[13,14] As in charge-transfer conductors, where the presence of sulfur and/or its heavier congener selenium imparts both softness (a lower U) and increased orbital overlap (a larger t and W) to donors such as tetrathiafulvalene,[15] so too does their incorporation into the framework of organic radicals. This greater overlap comes at a cost, however, as it also increases the tendency for the radicals to dimerize, with consequent loss of potential charge carriers. Thus, in the absence of steric blockage, early generations of S/Se-based heterocyclic radicals were strongly associated in the solid state,[16] and displayed insulating or weakly semiconducting behavior.[17] Improvements in conductivity could be induced by p-type doping,[18] which lowered U by changing the degree of band filling, but the challenge to reduce U and to prevent dimerization in purely neutral systems required greater spin delocalization, as per Haddon's original prescription.

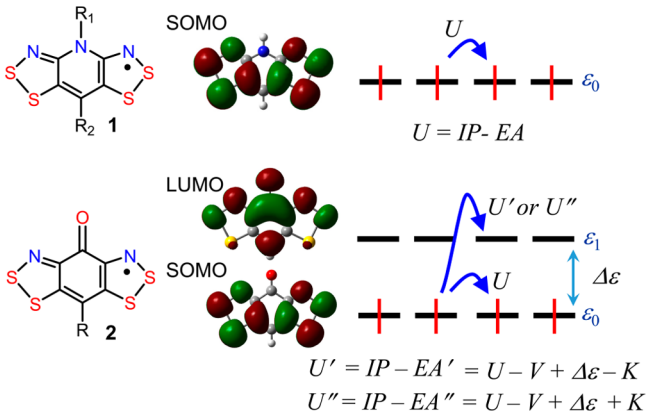

Figure 1. Resonance-stabilized bisdithiazolyl radicals **1** and **2** ($R_1 = R_2 = R = H$), showing the Kohn–Sham frontier orbitals and Coulombic barriers to intersite charge transfer along a chain of radicals, to generate anions with closed shell singlet (U), triplet (U') and open shell singlet (U'') states. The latter two (for **2**) are defined in terms of the SOMO-LUMO energy separation $\Delta\varepsilon$, the electron repulsion V between electrons in different orbitals on the same site, and the electron exchange term K.

Resonance stabilized heterocyclic radicals, in which spin density is equally partitioned between heterocycles, were developed to address the delocalization challenge.[19] For example, in the two bisdithiazolyls **1** and **2** shown in Figure 1, the radical SOMO and hence unpaired spin density spans the entire molecule, regardless of the nature of the bridging unit, be it an *N*-alkylpyridine ring in **1**[20] or an oxobenzene moiety in **2**.[21] Initial work on derivatives of **1** confirmed that their conductivity was improved (the Mott state was destabilized) by virtue of a lowered Coulombic barrier (U) to charge transfer, expressed in terms of the difference between the ionization energy (IP) and electron affinity (EA) of the radical. At the same time spin delocalization helped suppress pancake[22] dimerization. While they were still Mott insulators, with charge gaps $\Delta_C = U - W$ between the Mott insulating and metal states near 0.5 eV, replacement of sulfur by its heavier congener selenium reduced the value of Δ_C substantially,[23] to the point that "bad metal" states could be accessed under relatively mild applied pressure.[24] The selenium-based variants also displayed strong isotropic and anisotropic magnetic exchange interactions, which gave rise to magnetically ordered phases with relatively high ordering temperatures and coercive fields.[25,26]

Charge transport in oxobenzene-bridged radicals **2** is improved relative to **1** by so-called multiorbital effects, which arise from the interaction of the LUMO of the carbonyl group with the π-system of the radical, and consequent introduction of a low-lying π-LUMO.[27] The presence of this extra orbital increases the electronic and magnetic degrees of freedom available for transfer of the unpaired electron, by reducing U to U' or U'', the latter two being equal to $U - V + \Delta\varepsilon \pm K$, where $\Delta\varepsilon$ is the SOMO-LUMO gap, V represents the repulsion between electrons in different orbitals, K is the electron exchange term, and the sign of K reflects formation of a triplet (−ve) or open shell singlet (+ve) anion. Density Functional Theory (DFT) calculations suggest that $U' < U'' < U$, that is, the triplet anion is energetically favored, a feature which enhances ferromagnetic exchange interactions and promotes magnetic ordering at low temperatures.[28] With respect to charge transport, the effect of the low-lying LUMO is to reduce U to U' or U'', and thereby destabilize the Mott insulating state. The resulting decrease in charge gap Δ_C allows for higher conductivities and lower thermal activation energies E_{act} than **1**. Further reduction and eventual closure of the charge gap Δ_C can be achieved by the application of relatively mild pressure, with metallization for R = H, F, Ph observed at pressures ranging from 3 to 12 GPa.[29] In the case of R = F, Fermi liquid behavior has been identified near 6 GPa.[29] To a large extent the variations in the solid state properties within this family of radicals can be attributed to differences in electronic dimensionality. For example, when R = H, the radicals are aligned in relatively 1D slipped π-stack arrays,[21e] while for R = F, the radicals adopt a classic brick wall architecture,[21d] and the resulting 2D electronic structure[29] is more conducive to stabilization of a metallic state.

In addition to their role in influencing crystal packing, the exocyclic ligand R in oxobenzene-bridged radicals **2** can also play an important role in determining the magnitude of U. In *N*-alkylpyridine-bridged radicals **1** this is not the case; U is largely independent of nature of the ligands R_1/R_2, as the SOMO is nodal at the sites of substitution.[19] While the same situation also applies in oxobenzene-bridged radicals **2**, that is, the SOMO is nodal at the sites of substitution, the LUMO is *not*;[27] to a first approximation its orbital energy ε_1 should therefore be raised (or lowered) depending on the π-electron releasing (or accepting) power of the basal R-group. The implication of this idea is that the SOMO-LUMO separation $\Delta\varepsilon$ and hence the values of U' and U'' should be tunable. Notwithstanding the vagaries of crystal packing and resulting bandwidth issues, improvements in performance at the solid state level in oxobenzene-bridged radical **2** should therefore be attainable simply by molecular modification, that is, by judicious choice of R-group. Herein we demonstrate the validity and utility of this concept by examining the molecular and solid state transport properties of the nitro-substituted radical **2a** (**2**, R = NO_2). The presence of this strong π-electron withdrawing NO_2 group leads to a reduction in the magnitude of U' (U'') relative to U, and the generation of a material with a near metallic ground state.

RESULTS AND DISCUSSION

Synthesis. Preparation of the nitro-substituted oxobenzene-bridged bisdithiazolyl **2a** (Scheme 1) begins with the stepwise reduction of picric acid **3**, first using ammonium polysulfide to generate 2-amino-4,6-dinitrophenol **4**,[30] and then L-ascorbic acid to effect the second reduction to 2,6-diamino-4-nitro-

DOI: 10.1021/jacs.6b11779
J. Am. Chem. Soc. 2017, 139, 1625−1635

Scheme 1

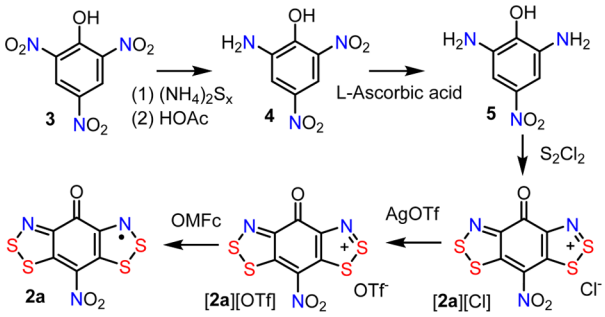

phenol **5**.[31] Finally, double Herz cyclocondensation[32] of **5** with sulfur monochloride in acetonitrile affords the desired oxobenzene-bridged bisdithiazolylium framework in the form of the black, insoluble chloride salt [**2a**][Cl]. Metathesis of this crude material with silver triflate (AgOTf) in hot acetonitrile affords a deep red solution (λ_{max} = 505 nm) of the corresponding triflate salt [**2a**][OTf], which crystallizes upon cooling as lustrous green shards.

Chemical reduction of [**2a**][OTf] to the neutral radical can be effected using octamethylferrocene (OMFc) in acetonitrile (MeCN) or propionitrile (EtCN) solution. As with other oxobenzene-bridged bisdithiazolyls,[21c,f] there is a marked tendency for **2a** to crystallize as a solvate. Thus, when acetonitrile is employed, black needles of the 1:1 solvate **2a**·MeCN are produced, while with propionitrile, black plates of the 4:1 solvate, that is, **2a**·1/4EtCN, are formed. The structural identity of both materials has been established by single crystal X-ray diffraction, but the formulations are also supported by elemental analysis and, in the case of **2a**·MeCN, by thermogravimetric analysis (see Figure S1), which shows a rapid weight reduction starting near 70 °C corresponding to the loss of one MeCN molecule per radical unit. Differential scanning calorimetry show a single phase transition at the same temperature range.

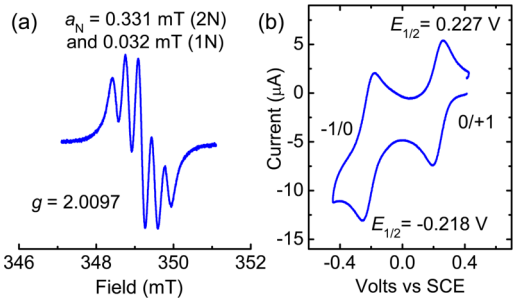

Figure 2. (a) X-Band EPR spectrum of **2a** in toluene at ambient temperature. (b) CV scan of [**2a**][OTf] in MeCN, with Pt electrodes, 0.1 M n-Bu_4NPF_6 electrolyte, scan rate 100 mV s^{-1}.

EPR Spectroscopy, Electrochemistry and Ion Energetics. The electronic structure of **2a** has been probed at the molecular level by EPR spectroscopy, cyclic voltammetry and computational methods. The X-band EPR spectrum (g = 2.0097) in toluene (Figure 2a) displays the expected pentet fine structure pattern arising from hyperfine coupling (a_N = 0.331 mT) to the two equivalent ^{14}N nuclei (I = 1) within the heterocyclic framework; weaker, unresolved coupling (a_N = 0.032 mT) to the nitro group can be extracted by spectral simulation. These values are similar to those seen in related oxobenzene-bridged related radicals, notably **2b,c** (**2**, R = H, F),[21d,e] and are consistent with estimates obtained from DFT calculations (Table 1). Taken collectively, the results indicate little dependence of the value of the spin distribution on the nature of the basal ligand, a conclusion consistent with the fact that the radical SOMO is nodal at the site of substitution.

Table 1. Hyperfine Coupling Constants, Electrochemical Potentials and Ion Energetics

radical	**2a**, R = NO_2	**2b**, R = H	**2c**, R = F
a_N, mT[a]	0.331 (0.234)	0.354 (0.277)	0.333 (0.277)
a_R, mT[a]	0.032 (0.045)	0.203 (0.372)	0.674 (0.837)
$E_{1/2}^{(-1/0)}$, V[b]	−0.218	−0.525[c]	−0.479[c]
$E_{1/2}^{(0/+1)}$, V[b]	0.227	0.035	0.208
E_{cell}, V	0.45	0.56[d]	0.69[d]
IP, eV[e]	4.852	4.610	4.784
EA, eV[e]	3.632	3.376	3.542
EA′, eV[e]	4.160	3.787	3.825
EA″, eV[e]	4.045	3.569	3.658
U (eV)[e]	1.220	1.234	1.242
U′, eV[e]	0.692	0.822	0.959
U″, eV[e]	0.806	1.041	1.126

[a]Observed hyperfine coupling constants a_N and a_R (R = $^{14}NO_2$, ^1H and ^{19}F), with calculated (U)B3LYP/6-311G(d,p) values in parentheses. [b]Volts versus SCE. [c]Reduction to the anion is irreversible, E_{pc} values are cited. [d]E_{cell} estimated from difference in E_{pc} values. [e](U)B3LYP/6-311G(d,p)/PCM calculated values, with MeCN as solvent. Values of *EA*, *EA′* and *EA″* refer respectively to formation of the closed shell singlet, triplet and open shell singlet anion (see Figure 1); *U*, *U′* and *U″* follow suit. Data for R = H and F are from refs 21d, f, and 27.

In contrast to the EPR data, which reflect a similar ground state structure, the three radicals **2a,b,c** display significant differences in their electrochemical properties. While the cationic and anionic states can be easily generated electrochemically for all three radicals, the cell potentials E_{cell}[33] are markedly dependent on the nature of the R-group. For example, cyclic voltammetry on a solution of [**2a**][OTf] in MeCN (Figure 2b) indicates two reversible waves, the +1/0 couple with $E_{1/2}$ = +0.227 V vs SCE and the −1/0 couple with $E_{1/2}$ = −0.218 V vs SCE. The resulting value for E_{cell} = 0.45 V is the lowest ever observed for a radical of this type (Table 1); those for **2b** and **2c** are some 100 and 200 mV higher, respectively.[21d,f] Such variations are not observed in the E_{cell} values of *N*-alkyl-bridged bisdithiazolyls **1**, which are uniformly higher and independent of the nature of the R_2-group.[19]

The reason for the marked dependence of E_{cell} of **2** on the nature of the R-group can be understood by considering the different anionic states accessible upon reduction. To demonstrate this point, we have carried out DFT calculations at the (U)B3LYP/6-311G(d,p)/PCM level to determine *IP*, *EA*, *EA′* and *EA″* values of **2a,b,c**, and hence the respective (solvent screened) Coulombic barriers *U*, *U′* and *U″*. The results, summarized in Table 1, indicate that the value of *U*, which corresponds electrochemically to formation of the closed shell singlet anion, or a SOMO-to-SOMO electron transfer in the solid state, remains essentially constant across the series. By contrast reduction to a triplet or open shell singlet anion (*EA′* and *EA″* respectively), corresponding to a SOMO-to-LUMO transfer in the solid state, becomes increasingly easier along the series R = F < H < NO_2, in keeping with the expected changes

DOI: 10.1021/jacs.6b11779
J. Am. Chem. Soc. 2017, 139, 1625−1635

in the SOMO-LUMO gap $\Delta\varepsilon$ occasioned by the π-electron donating/releasing power of the R-group. At the DFT level, the triplet anion is preferred over the open shell singlet for all three radicals, so that $U' < U''$, but regardless of this ordering, the observed trends in the values of E_{cell} of **2a**,**b**,**c** can be viewed as a confirmation of the involvement of the LUMO of the radical in defining the nature and accessibility of the anionic state, and hence the value of E_{cell}, a feature not possible for **1**. Taken together, the electrochemical and computational results support the idea that, in contrast to **1**, the solid state Coulombic barrier in **2** is not only small, but *tunable*; the value of U_{eff} (the composite of U, U' and U'') is increased relative to R = H by π-donor ligands (R = F) and decreased by π-acceptor ligands (R = NO_2). On this basis, it can be reasoned that **2a** represents a promising building block for a neutral radical-based metal.

Table 2. Crystal Data

	2a·MeCN	**2a**·1/4EtCN
formula	$C_6N_3O_3S_4{\cdot}C_2H_3N$	$4(C_6N_3O_3S_4){\cdot}C_3H_5N$
fw	331.38	1216.40
a, Å	3.4719(3)	25.0506(2)
b, Å	30.764(4)	23.9588(2)
c, Å	11.0663(13)	14.9339(2)
β, deg	90.2099(7)	117.7784(5)
V, Å^3	1182.0(2)	7930.13(14)
ρ(calcd), g cm^{-3}	1.862	2.038
space group	$P2_1/n$	$C2/c$
Z	4	8
temp, K	100(2)	296(2)
μ, mm^{-1}	0.811	0.955
λ, Å	0.71073	0.71073
solution method	direct methods	direct methods
R, R_w (on F^2)	0.0360, 0.0757	0.0430, 0.0731

Ambient Pressure Crystallography. As described above, crystallization of **2a** by in situ reduction of the triflate salt [**2a**][OTf] in MeCN and EtCN, affords the solvates **2a**·MeCN and **2a**·1/4EtCN respectively. The crystal structures of these two materials have been determined by single crystal diffraction; crystal data are provided in Table 2. Black needles of **2a**·MeCN belong to the monoclinic space group $P2_1/n$, and consist of slipped π-stacks of evenly spaced radicals running parallel to the *a*-axis (Figure 3); there is no indication of a charge density wave (CDW) or Peierls distortion.[34] The associated tilt angle (τ = 76.4°) with respect to the stacking direction and mean-plane separation (δ = 3.374 Å) of neighboring radicals are consistent with nearly direct superposition of radicals along the stacking direction. Each radical is coordinated laterally to an acetonitrile molecule by a pair of short (inside the van der Waals separation)[35] S···N′ contacts, in a fashion similar to that found in **2**·MeCN (R = Cl, Br, I)[21c,f] and **2**·EtCN (R = I).[21f] There is also a network of close intermolecular S···O′ and S···N′ interactions that connect adjacent radicals along the *n*-glides to produce a ruffled ribbon arrangement running parallel to the *c*-axis. This pattern is reminiscent of the packing observed in **2b**.[21e] Intramolecular bond lengths and angles are nominal.

The crystal structure of **2a**·1/4EtCN belongs to the monoclinic space group $C2/c$, and with Z = 8 there are four independent molecules (A–D) in the asymmetric unit, which consists of an approximately planar pinwheel arrangement of four radicals, as shown in Figure 4a; the nitrogen atom of the

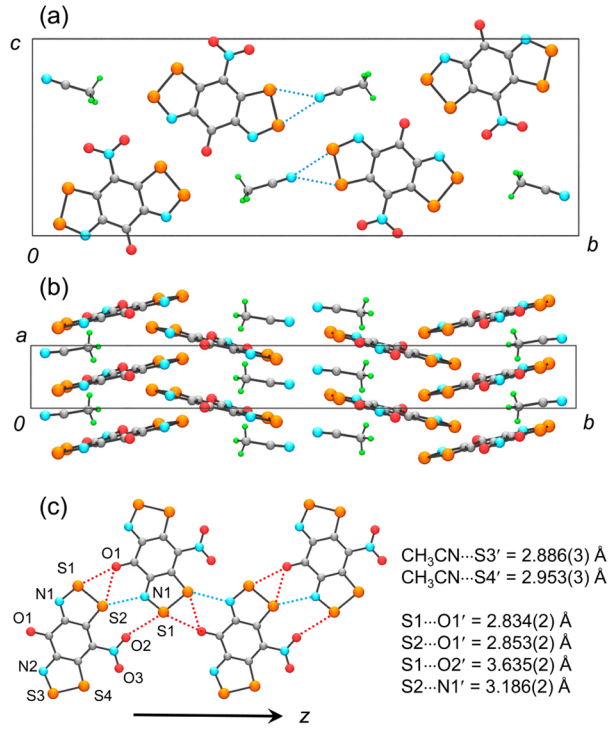

Figure 3. (a) Unit cell drawing of **2a**·MeCN, viewed parallel to the *a*-axis. (b) Out-of-register slipped π-stacking of radicals. (c) Ribbon-like arrays of radicals running parallel to the *c*-axis, and intermolecular contacts.

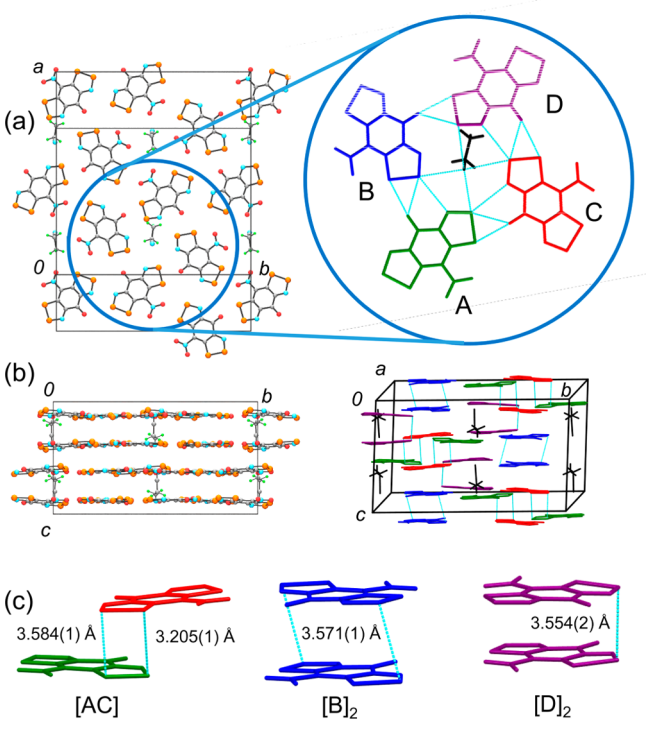

Figure 4. (a) Unit cell of **2a**·1/4EtCN, and pinwheel arrangement of the asymmetric unit in the *ab* plane. (b) Side-on views of the unit cell of **2a**·1/4EtCN, showing 4-decker repeat unit, and association of individual radicals into [AC], $[B]_2$ and $[D]_2$ dimers. (c) Local views of dimers, with intermolecular S–S distances.

single EtCN solvent molecule is located at the center of this pinwheel. Within each pinwheel there is a spider-web like

DOI: 10.1021/jacs.6b11779
J. Am. Chem. Soc. 2017, 139, 1625–1635

network of close (inside van der Waals separation)[35] S···O′ and S···N′ interactions (listed in Figure S3), which creates a slightly ruffled layer of radicals lying parallel to the *ab* plane. There are four such layers stacked along the *c*-direction in the unit cell (Figure 4b), with nearest neighbor layers related by 2-fold rotations, and second nearest layers related by *c*-glides. Radicals in different layers within this 4-decker structure are linked into three unique dimer pairs (Figure 4c) via one or more close S−S bonds, with radicals A and C overlapping to form [AC] heterodimers, while radicals B and D associate as $[B]_2$ and $[D]_2$ homodimers.

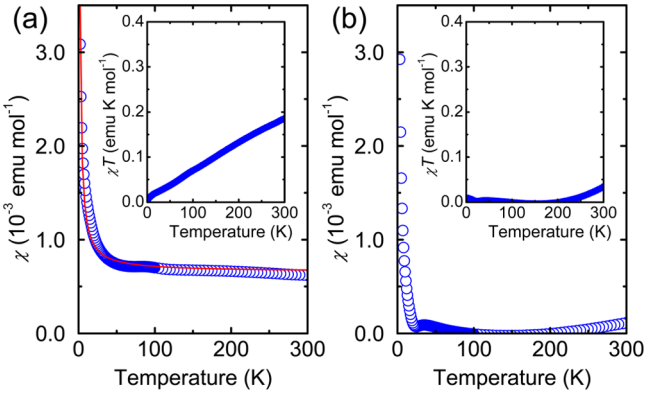

Figure 5. Plots of χ vs T and χT vs T (inset) at a field H = 1000 Oe for (a) on **2a**·MeCN and (b) **2a**·1/4EtCN. A nonlinear fit (in red) to the data for **2a**·MeCN affords a Curie defect concentration of 1.7% and $\chi_{TIP} = 6 \times 10^{-4}$ emu mol^{-1}.

Magnetic Susceptibility Measurements. The results of variable temperature magnetic susceptibility (χ) measurements on **2a**·MeCN and **2a**·1/4EtCN, performed over the range 2−300 K at a field H = 1000 Oe, are presented in Figure 5 in the form of plots of χ and χT (corrected for diamagnetic contributions) versus T. In the case of **2a**·MeCN the magnetic profile shows no indication of a phase transition to a Peierls distorted (CDW) or to a magnetically ordered state. Instead, the material displays weak temperature independent paramagnetism (TIP) over the entire temperature range, with a small Curie tail apparent at low temperature that may arise from defects. From a nonlinear Curie fit the concentration of these defects is estimated to be near 2%. The derived value for $\chi_{TIP} = 6 \times 10^{-4}$ emu mol^{-1} is suggestive of Pauli paramagnet behavior, with a magnitude similar to that found in organic charge transfer salts,[36] spiro-bisphenalenyl[12] and metal-bridged bis-dithiolate radicals[37] possessing a near metallic state.

In accord with the presence of four weakly associated dimers in its crystal structure, the magnetic profile for **2a**·1/4EtCN points to essentially diamagnetic behavior, with a weak Curie tail at low temperature arising from defects, but otherwise a near zero value of χ up to 200 K, and a very slight increase thereafter (more readily seen in the χT versus T plot). The latter feature probably reflects a gradual, thermally driven increase in the degree of dimer dissociation.

Conductivity Measurements. We have performed 4-probe, variable temperature conductivity measurements on pressed pellet samples of both **2a**·MeCN and **2a**·1/4EtCN. Given the relatively large size and needle-like morphology of crystals of **2a**·MeCN, we also attempted measurements on single crystals. However, not only were the needles extremely fragile, but attachment of wires with silver paint caused

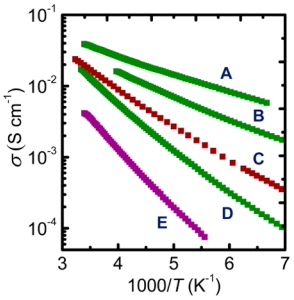

Plot	Radical	σ_{RT}, S cm^{-1}	E_{act}, eV
A	**2a**·MeCN	4 × 10^{-2}	0.05
B	**2a**·MeCN	2 × 10^{-2}	0.09
C	**2c** (R = F)	2 × 10^{-2}	0.10
D	**2a**·¼ EtCN	2 × 10^{-2}	0.14
E	**2b** (R = H)	6 × 10^{-3}	0.16

Figure 6. Plots of σ vs 1000/T for radicals **2a,b,c** (R = NO_2, H, F), from measurements using 4-probe technique on pressed pellet samples, with derived thermal activation energies E_{act}. For **2a**·MeCN, results from 2-probe single crystal measurements (A) are also provided. Data for **2b,c** are from refs 21d, e.

significant deterioration of the surface of the crystals, possibly as a result of desolvation (loss of MeCN). We were, however, able to perform 2-probe single crystal measurements, and these results, along with those obtained using the 4-probe technique on pressed pellets, are shown in Figure 6. By way of comparison, the corresponding data (4-probe, pressed pellet) for **2b,c** are illustrated; thermal activation energies E_{act} are also provided. Overall, the results indicate a high, albeit activated conductivity for **2a**·MeCN. Indeed its performance is the best seen to date for a heterocyclic radical conductor, with a room temperature conductivity σ_{RT} slightly higher and E_{act} slightly lower than that of **2c** (the previous best).[21d] The dimerized solvate **2a**·1/4EtCN also shows good charge transport behavior for a closed shell semiconductor.

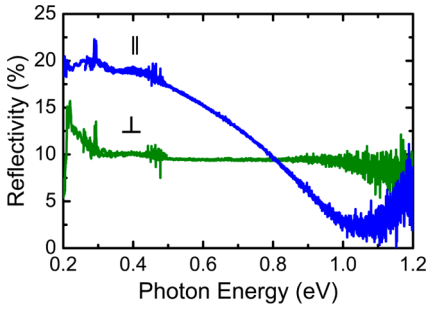

Figure 7. Single crystal reflectivity of **2a**·MeCN at ambient pressure, measured using incident radiation polarized parallel (||) and perpendicular (⊥) to the *a*-axis (the needle direction).

While we experienced difficulties obtaining single crystal conductivity data on **2a**·MeCN, measurements of polarized infrared reflectance spectra on single crystals proved more successful. Figure 7 shows the reflectivity obtained from the flat face of a needle, with incident radiation polarized parallel (||) and perpendicular (⊥) to the needle direction, which corresponds to the π-stacking *a*-axis. With light polarized || to the *a*-axis the response in reflectivity is Drude-like, with a pronounced minimum in reflectivity near 1 eV, which may be assigned to a plasma edge, followed by a rapid increase. By contrast, with polarization ⊥ to the *a*-axis, reflectivity is weak and featureless. Overall this response is consistent with the behavior of 1D metallic charge transfer salts.[38]

High Pressure Structural and Conductivity Measurements. Given the impressive ambient pressure transport property data on **2a**·MeCN, that is, the Pauli paramagnet-like

DOI: 10.1021/jacs.6b11779
J. Am. Chem. Soc. 2017, 139, 1625−1635

temperature dependence of its magnetic susceptibility, and its high conductivity coupled with a small activation energy, we wished to explore the effect of applied pressure on its performance. At what pressure might a metallic state be observed? As a first step in this direction, however, we needed to establish the effect of pressure on the crystal structure itself. Given the proclivity of the material to lose solvent by heating to just 70 °C, we were concerned that pressure might also lead to a loss of solvent, and hence deterioration in crystallinity and conductivity.

High-pressure (HP) crystallographic studies were therefore performed on **2a**·MeCN, using synchrotron radiation and diamond anvil cell (DAC) techniques. Powder diffraction data were collected at room temperature as a function of increasing pressure up to 8 GPa. The retention of resolution and the smooth and steady evolution of the positions of the diffraction peaks with increasing pressure indicated that neither sample degradation (solvent loss) nor phase change was occurring over this pressure range. A series of data sets so obtained were indexed, and the structures solved and refined in DASH using a rigid body molecular model of the radical taken from the single crystal structure solution. Initial attempts to include the solvent molecule in the model were eventually abandoned, as its presence did not affect the outcome of the refinement. During the final Rietveld refinements (in GSAS) only the unit cell parameters were optimized; a sampling of the crystal data at selected pressures is provided in Table S1. Variations in the unit cell dimensions as a function of pressure are shown in Figure 8a. All three axes contract, the most significant response being parallel to the stacking direction (the *a*-axis), as found previously for **2b** and **2c**,[29] an observation which reflects the relative ease of compression of the layered π-stacks.

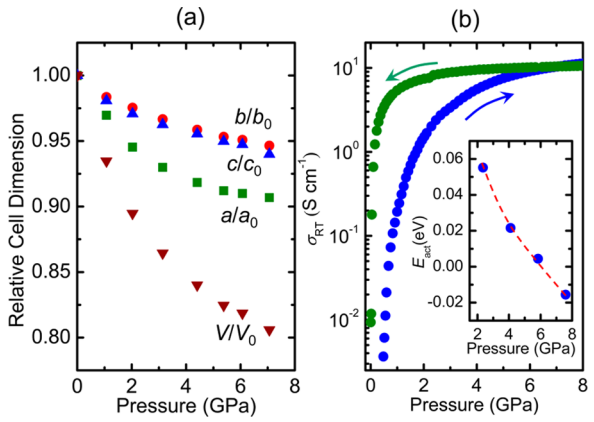

Figure 8. (a) Contraction in unit cell dimensions of **2a**·MeCN over the pressure range 0−8 GPa. (b) Pressure dependence of the room temperature conductivity σ_{RT} of **2a**·MeCN during compression (blue) and decompression (green). The inset shows the pressure dependence of the thermal activation energy E_{act}, measured over the range −50 °C to +20 °C.

Given the well-behaved structural response of **2a**·MeCN to physical pressure, we carried out high pressure conductivity measurements using multianvil press techniques. Data collected at room temperature in both compression and decompression modes over the pressure range 0−8 GPa are shown in Figure 8b. We attribute the initially low value of σ_{RT} observed during compression to grain boundary effects arising from incomplete compaction of the sample. With increasing pressure there is a rapid rise in conductivity up to ∼5 GPa, then a more gradual increase thereafter, with σ_{RT} reaching 10^1 S cm^{-1} at 8 GPa. Although this limiting value lies well below the Mott−Ioffe−Regel limit for a metallic state,[39] it is similar in magnitude to that observed upon compression of related radicals, and may be ascribed to the formation of a highly correlated or "bad metal" state. Upon decompression, the high pressure limiting value of σ_{RT} is maintained down to near 1 GPa, whereupon it rapidly drops to near 10^{-2} S cm^{-1}, that is, close to the value obtained from the ambient pressure 4-probe measurements. While this delay in recovery may stem from clamping of the sample, it may also reflect the elimination of grain boundaries during compression, so that the "bad metal" state is in fact preserved down to near 1 GPa. The results of separate measurements of the thermal activation energy E_{act}, performed over the temperature range −50 °C to +20 °C (in order to avoid solvent loss), were consistent with the conductivity measurements. Thus, as illustrated in the inset to Figure 8b, E_{act} steadily decreases with increasing pressure, and is essentially eliminated near 6 GPa, heralding closure of the charge gap Δ_C and formation of bad metal state.

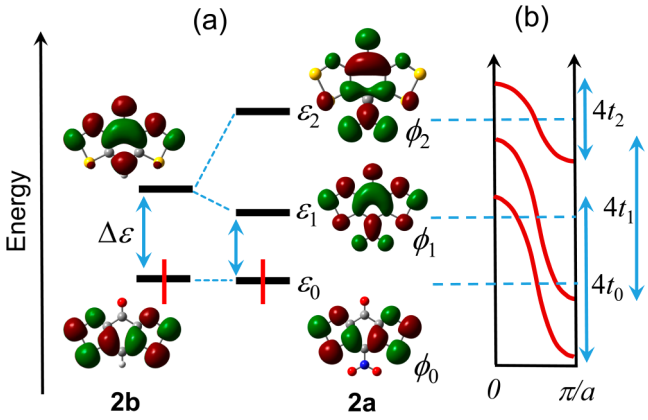

Figure 9. (a) Frontier Kohn−Sham π-MOs of **2a** and **2b**, and energy level sketch (not to scale) illustrating the orbital energy changes occasioned by the incorporation of the NO_2 group. (b) Dispersion of CO energy bands arising from a single π-stacked array of **2a**.

Band Structure Calculations. The relatively high conductivity and diamagnetic behavior of **2a**·1/4EtCN militate in favor of a small band gap semiconductor description, but with four molecules in the asymmetric unit, its unit cell is too large and the resulting solid state electronic structure too complex to allow a detailed theoretical examination. By contrast, the 1D π-stacked architecture of **2a**·MeCN is more amenable to both qualitative and quantitative analysis. To begin such an exercise, it is useful to identify the relevant frontier molecular orbitals of the building block **2a**, which are easily derived from those of the prototypal radical **2b** (Figure 9a). While attachment of a nitro group does not, to first order, perturb the SOMO (ϕ_0, energy ε_0), the LUMO in **2a** is split into a new LUMO (ϕ_1, energy ε_1), which is lowered in energy relative to **2b** and based largely on the heterocycle, and a higher lying LUMO+1 level (ϕ_2, energy ε_2), which is more localized on the nitro group. The idealized band structure arising from a perfectly superimposed 1D π-stacked array of **2a** can then be easily anticipated. The three MOs ϕ_{0-2} will generate three largely unhybridized crystal orbitals (COs), whose individual bandwidths will reflect the relative magnitude of the respective

DOI: 10.1021/jacs.6b11779
J. Am. Chem. Soc. 2017, 139, 1625−1635

π-stack hopping integrals t_{0-2}. Because ϕ_0 and ϕ_1 are both heterocycle-centered, the values of $t_{0,1}$ should be comparable, and both are expected to be numerically larger than t_2, which arises from interactions between orbitals that are primarily ligand-based.

To quantify this description we have performed single point DFT band structure calculations with the Quantum Espresso package, using atomic coordinates taken from crystal structures determined at ambient and elevated pressure; to simplify the analysis the solvent molecules were not included. The results of the 0 GPa calculation, based on a nonmagnetic state, are shown in Figure 10a in the form of a CO band dispersion diagram over several reciprocal space directions within the first Brillouin zone. The pattern of bands near the Fermi surface follows directly from frontier orbital and CO ordering described above (Figure 9), with three bands each comprised of four COs arising from the SOMO (ϕ_0), LUMO (ϕ_1) and LUMO+1 (ϕ_2). It is immediately evident that the electronic structure is very 1D, as expected from the crystal structure and the optical response, with strong band dispersion of the ϕ_0 and ϕ_1 bands (~1 eV) from $\Gamma \rightarrow$ X, loosely speaking the π-stacking direction, and virtually none along $\Gamma \rightarrow$ Y, $\Gamma \rightarrow$ Z vectors, that is, corresponding to interactions transverse to the stacking axis. The nonintersecting appearance of these two bands is in marked contrast to the band structure of **2c**, where the 2D packing of radicals gives rise to strong mixing (hybridization) of the COs.[28a] Given the position of the Fermi level it is nonetheless clear that both ϕ_0 and ϕ_1 bands are both partially occupied, giving rise to a less than 1/2-filled band description, although the involvement of the latter is significantly less. As expected the ϕ_2 band is relatively narrow, and separated from the lower-lying ϕ_0 and ϕ_1 bands. The effect of pressure on the electronic structure of **2a** is illustrated in Figure 10b, which shows the band structure at 4.4 GPa. It is immediately apparent that the 1D nature of the material is preserved under pressure; band dispersion from $\Gamma \rightarrow$ X increases slightly with compression along the stacking axis, but there remains little or no dispersion along $\Gamma \rightarrow$ Y or $\Gamma \rightarrow$ Z.

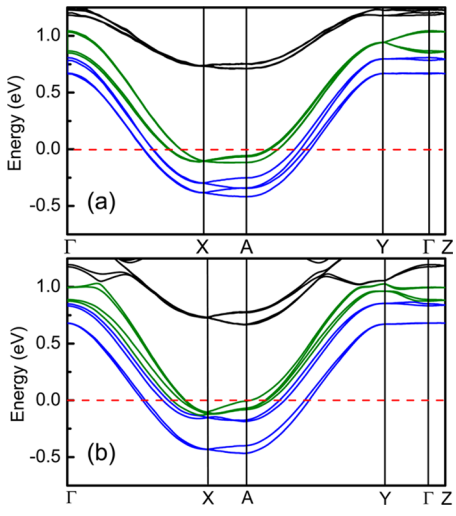

Figure 10. DFT computed band structure of **2a**·MeCN at (a) 0 GPa and (b) 4.4 GPa, showing dispersion of bands based on unhybridized COs arising from the SOMO (ϕ_0) in blue, the LUMO (ϕ_1) in green and LUMO+1 (ϕ_2) in black. The Fermi level is shown with a dashed red line.

SUMMARY AND CONCLUSIONS

Historically, achieving high conductivity in purely organic radical-based molecular materials has been impeded by the energetic imbalance between the high potential energy cost (U) of site-to-site transfer of an unpaired electron and the limited kinetic stabilization (W) afforded by charge delocalization into a half-filled energy band. To break out of the Mott insulating state that this condition imposes, a variety of approaches have been pursued. The use of spin delocalization to lower U, as Haddon originally proposed,[2] and the incorporation of heavy heteroatoms (chemical pressure) to increase W,[13,14] have both been extensively explored. Performance can also be improved by relaxing the classical one-orbital, one-electron model, as in mixed-valence spiroconjugated PLYs[9,10] and doped radical ion salts,[18] in which the effective Coulombic barrier is reduced as additional channels for charge transport become available.

In the case of oxobenzene-bridged bisdithiazolyls **2** improved conductivity arises from a multiorbital effect, that is, the presence of a low-lying LUMO (Figure 1) which destabilizes the Mott state by generating a lower effective Coulombic barrier U_{eff}.[27] In some cases, such as **2c**, the 2D electronic structure allows for mixing (hybridization) of the SOMO and the LUMO, which leads to an enhanced kinetic stabilization E_k of the metallic state occasioned by a lowering the Fermi level relative to that of the Mott state.[28a,29] Together or separately, these two effects contribute to reducing the charge gap $\Delta_C = U_{eff} - E_k$. In this respect these materials provide an interesting parallel with neutral, nominally radical (S = 1/2) Au(III) bisdithiolate complexes, where a high-lying HOMO may play a similar role.[37,40]

In addition to structural modifications, which can reduce the charge gap Δ_C by increasing electronic dimensionality and hence E_k, the performance of multiorbital radicals **2** can, in principle, be improved through a lowering of U_{eff}. In this work we have demonstrated that significant changes in E_{cell}, the electrochemical signature of U_{eff}, can be induced by substituent effects, that is, by attachment of a strongly electron withdrawing nitro-group (R = NO_2). However, while the ion energetics of **2a** suggest that it should serve as an excellent building block for a radical-based metal, our attempts to incorporate it into a crystalline lattice have yielded the two solvates **2a**·MeCN and **2a**·1/4EtCN, neither of which represents, from a *structural* perspective, an ideal candidate for a radical-based metal. In the 1/4 EtCN solvate the radicals are dimerized, and while they are not dimerized in the MeCN solvate, the almost directly superimposed, 1D π-stack packing pattern leads to a highly 1D electronic structure.

The transport properties of **2a**·MeCN are thus characteristic of the highly correlated "inter-regnum" region found between Mott insulating and metallic states, in which there is a separation of the spin and charge behavior of the unpaired electrons.[41] While the Pauli-like magnetic properties of this material are consistent with a metallic state, pressed pellet and single crystal measurements indicate thermally activated conductivity, with a small charge gap 0.05−0.10 eV which can be closed by the application of 6 GPa pressure. Polarized single crystal reflectance measurements confirm strong electronic anisotropy, a result supported by DFT band structure calculations, which support the highly 1D electronic structure description.

In summary, it is perhaps ironic that the structure of fluoro-substituted radical **2c** combines a somewhat larger E_{cell} with a

DOI: 10.1021/jacs.6b11779
J. Am. Chem. Soc. 2017, 139, 1625−1635

highly developed 2D-electronic structure, in essence the reverse combination of potential and kinetic energy terms found in **2a**·MeCN. The challenge for the future will be to design materials which enjoy *simultaneous* optimization of both terms, that is, to find the right building block *and* the right crystal structure.

EXPERIMENTAL SECTION

General Methods and Procedures. The reagents picric acid **3**, sulfur monochloride, silver triflate (trifluoromethanesulfonate), ammonium sulfide solution (40−48 wt %), L-ascorbic acid and octamethylferrocene (OMFc) were obtained commercially. All were used as received save for OMFc, which was sublimed in vacuo and recrystallized from acetonitrile prior to use. The solvents acetonitrile (MeCN), propionitrile (EtCN), dichloroethane (DCE), dichloromethane (DCM), carbon disulfide (CS_2), ethyl acetate (EtOAc), glacial acetic acid (HOAc) were of at least reagent grade. MeCN was dried by distillation from P_2O_5 and CaH_2 before use. EtCN was purified by prewashing with aqueous HCl, then dried over K_2CO_3 and molecule sieves, followed by distillation from CaH_2.[42] All reactions were performed under an atmosphere of dry nitrogen. Melting points are uncorrected. Infrared spectra (Nujol mull, KBr optics) were recorded on a Nicolet Avatar FTIR spectrometer at 2 cm^{-1} resolution, and UV−visible spectra were collected on samples dissolved in MeCN using a PerkinElmer Lambda 35 UV−vis spectrophotometer. ^1H NMR spectra were run on a Bruker Avance 300 MHz NMR spectrometer, and low resolution Electro-spray Ionization (ESI) mass spectra were recorded on a Micromass Q-TOR Ultima Global LC/MS/MS system. Elemental analyses were performed by MHW Laboratories, Phoenix, AZ, 85018. Thermogravimetric analysis (TGA) and differential scanning calorimetry (DSC) on **2a**·MeCN was performed in a platinum crucible using a TA Instruments SDT Q600 under nitrogen gas with a heating (and cooling) rate of 1 °C min^{-1}.

Preparation of Ammonium 2-amino-4,6-dinitrophenolate.[30] Ammonium sulfide solution (50 mL) was added slowly over 20 min to a yellow solution of picric acid **3** (36.0 g, 0.157 mol) in 600 mL of 20% aq. NH_3 at 60 °C, while never allowing the temperature to exceed 70 °C, to give a deep red mixture. The mixture was heated for 3 h, and the resulting gray solid filtered off and washed with 300 mL of hot distilled H_2O. The filtrate was concentrated to a third of the volume in vacuo at 60 °C, then cooled on an ice-bath for 2 h, and the resulting dark purple needles collected by filtration. The crude product was boiled into 500 mL distilled H_2O, the mixture hot filtered and the filtrate concentrated in vacuo to 300 mL. The filtrate was allowed to cool to room temperature, whereupon 50 mL 28% aq. NH_3 was added and the mixture allowed to stand overnight. The dark purple-black needles of the ammonium salt of **4** were filtered off and dried in air. Yield 28.1 g, (0.130 mol, 83%). ^1H NMR (DMSO-d_6) δ: 8.153 (d, C−H, J_4 = 2.7 Hz, 1H), 7.012 (s, broad; NH_4^+, 4H), 6.955 (d, C−H, J_4 = 2.7 Hz, 1H), 5.087 (s, broad; N−H, 2H). IR (cm^{-1}): 3407 (m), 3313 (w), 3277 (br, m), 3158 (br, m), 1614 (sh, m), 1589 (m), 1537 (s), 1311 (s), 1262 (br, vs), 1189 (w), 1123 (w), 1069 (m), 997 (vw), 936 (w), 888 (w), 856 (w), 828 (w), 734 (m), 707 (w), 558 (w), 486 (m).

Preparation of 2-Amino-4,6-dinitrophenol 4.[31] Glacial acetic acid (20 mL) was added dropwise to a stirred solution of ammonium 2-amino-4,6-dinitrophenolate (18.9 g, 87.4 mmol) in 250 mL warm H_2O (~60 °C). The mixture was cooled on an ice−water bath and the resulting orange precipitate of **4** was collected by filtration and air-dried. Yield: 15.7 g (78.8 mmol, 79%). The product was recrystallized from EtOAc as orange needles, mp 169−171 °C. ^1H NMR ($CDCl_3$) δ: 11.178 (s, O−H, 1H), 8.392 (s, C−H, 1H), 7.730 (s, C−H, 1H), 4.478 (s, broad; N−H, 2H). IR (cm^{-1}): 3485 (m), 3470 (m), 3250 (br, s), 3117 (w), 3104 (w), 3072 (w), 1783 (w), 1615 (s), 1595 (s), 1557 (vs), 1507 (s), 1401 (m), 1338 (vs), 1299 (vs), 1233 (vs), 1141 (s), 1110 (s), 1064 (s), 994 (s), 934 (s), 895 (m), 880 (w), 855 (w), 816 (m), 804 (m), 771 (w), 736 (m), 725 (w), 711 (m), 675 (s), 569 (vw), 491 (w).

Preparation of 2,6-Diamino-4-nitrophenol 5. A mixture of 2-amino-4,6-dinitrophenol **4** (5.00 g, 25.1 mmol), L-ascorbic acid (22.2 g, 126.0 mmol), and a catalytic amount of $FeSO_4·7H_2O$ (0.80 g, 2.9 mmol) in 400 mL of 1.0 M NaOH was heated at 70 °C for 5 h. The deep red mixture was hot-filtered on a large Buchner funnel and cooled to 5 °C on an ice−water bath. Glacial acetic acid was added dropwise to the rapidly stirred, cold mixture, until pH ~ 5 was obtained. After 2 h a light brown solid was collected by filtration and air-dried. Recrystallization from hot H_2O afforded dark orange needles. Yield: 2.46 g (14.5 mmol, 58% yield); mp 168−169 °C. ESI MS (1:1 MeOH/H_2O + 0.1% formic acid) m/z = 170.08 ($M+H^+$). This material was dried at 100 °C in vacuo. Anal. Calcd for $C_6H_7N_3O_3$: C, 42.61; H, 4.17; N, 24.84. Found: C, 43.00; H, 4.37; N, 24.66. ^1H NMR (DMSO-d_6) δ: 6.883 (s, C−H), 5.890 (broad, N−H). IR (cm^{-1}): 3489 (m), 3471 (m), 3250 (br, s), 3121 (w), 3105 (w), 3077 (w), 1783 (w), 1635 (m), 1615 (m), 1595 (m), 1554 (s), 1516 (s), 1444 (m), 1401 (m), 1338 (vs), 1304 (s), 1237 (s), 1143 (m), 1112 (m), 1066 (m), 995 (m), 935 (m), 894 (w), 880 (w), 856 (vw), 817 (w), 806 (w), 771 (w), 736 (m), 712 (m), 676 (s), 590 (vw), 491 (w).

Preparation of [2a][Cl]. A solution of sulfur monochloride (4.0 mL, 6.8 g, 50.1 mmol) in 25 mL MeCN was added dropwise to a slurry of 2,6-diamino-4-nitrophenol (1.70 g, 10.0 mmol) in 200 mL MeCN and the mixture was heated under gentle reflux for 6 h. The black precipitate of crude [**2a**][Cl] was filtered off, washed with MeCN, hot DCE, CS_2 and DCM, then dried in vacuo, yield 2.29 g (7.03 mmol, 70%); mp >250 °C. IR (cm^{-1}): 1710 (s), 1626 (br, s), 1503 (vs), 1343 (m), 1291 (sh, m), 1277 (s), 1099 (vw), 1074 (w), 1017 (vw), 949 (w), 863 (w), 852 (w), 825 (w), 762 (m), 746 (w), 632 (vw), 613 (vw), 602 (vw), 568 (vw), 493 (m), 465 (w).

Preparation of [2a][OTf]. Silver triflate (4.10 g, 16.0 mmol) was added to a slurry of crude [**2a**][Cl] (4.55 g, 14.0 mmol) in 200 mL MeCN, to afford a deep red solution, which was heated at gentle reflux for 90 m, then filtered to remove gray-black precipitate of AgCl. The deep red filtrate was concentrated to 45 mL and crude [**2a**][OTf], a dark green-black solid, was collected by filtration. Recrystallization from MeCN afforded dark green shards (1.98 g, 4.50 mmol, 32%); mp >250 °C. Anal. Calcd for $C_7F_3N_3O_6S_5$: C, 19.13, N, 9.56. Found: C, 19.30; H, 0.1; N, 9.41. IR (cm^{-1}): 1692 (vs), 1515 (vs), 1402 (m), 1290 (s), 1246 (br, vs), 1224 (m), 1181 (m), 1157 (m), 611 (w), 574 (w), 520 (w), 502 (vw), 488 (w), 470 (w). UV−vis (MeCN), λ_{max} = 505 nm (log ε = 5.4).

Preparation of 2a·MeCN. *Method 1: Bulk Material for Conductivity and Magnetic Measurements.* A solution of [**2a**][OTf] (0.270 g, 0.614 mmol) in 100 mL of degassed MeCN (4 freeze−pump−thaw cycles) was combined with a solution of OMFc (0.240 g, 0.805 mmol) in 85 mL of similarly degassed MeCN to yield a dark blue solution with a dark green-black microcrystalline precipitate. After 30 min of stirring at room temperature, the microcrystalline product [**2a**][MeCN] was filtered off, washed with MeCN (4 × 20 mL) and dried in vacuo (0.145 g, 0.499 mmol, 81% yield); mp >250 °C. Anal. Calcd for $C_6N_3O_3S_4·(C_2H_3N)$: C, 29.00; H, 0.91; N, 16.91. Found: C, 28.80; H, 1.19; N, 16.78. IR (cm^{-1}): 1595 (br, vs), 1536 (br, s), 1490 (s), 1293 (br, vs), 1234 (s), 1129 (m), 1059 (m), 974 (w), 867 (m), 860 (sh, m), 812 (m), 758 (m), 738 (m), 635 (vw), 595 (w), 557 (w), 489 (m), 465 (w), 443 (w), 422 (w). Complete removal of MeCN solvent was effected by heating the solvate in vacuo at 90 °C for 30 m. Anal. Calcd for $C_6N_3O_3S_4$: C, 24.82; N, 14.47. Found: C, 25.00; H, trace; 14.11.

Method 2: Slow Diffusion for Single Crystals. A solution of [**2a**][OTf] (44 mg, 0.100 mmol) in 12 mL of degassed MeCN (4 freeze−pump−thaw cycles) was allowed to diffuse slowly into a similarly degassed solution of OMFc (32 mg, 0.107 mmol) in 15 mL MeCN over a 16 h period, affording [**2a**][MeCN] as lustrous green-black needles.

Preparation of 2a·1/4EtCN. A solution of [**2a**][OTf] (30 mg, 0.068 mmol) in 15 mL of degassed EtCN (4 freeze−pump−thaw cycles) was allowed to diffuse slowly into a similarly degassed solution of OMFc (28 mg, 0.094 mmol) in 15 mL EtCN over a 16 h period, affording **2a**·1/4EtCN as lustrous black plates suitable for both X-ray work and bulk property measurements. Anal. Calcd for $C_8H_3N_4O_3S_4.1/4(C_3H_5N)$: C, 26.66; H, 0.41; N, 14.97. Found: C, 26.59; H, 0.79; N, 15.00. IR (cm^{-1}): 1579 (br, s), 1491 (m), 1292 (s), 1224 (s), 1112 (w), 1058 (m), 860 (s), 808 (m), 723 (s), 559 (m).

DOI: 10.1021/jacs.6b11779
J. Am. Chem. Soc. 2017, 139, 1625−1635

Cyclic Voltammetry. Cyclic voltammetry was performed using a PINE Bipotentiostat, Model AFCClBP1, with scan rates of 50−250 mV s^{-1} on a solution of [**2a**][OTf] in anhydrous MeCN degassed with argon and containing 0.1 M tetra-*n*-butyl-ammonium hexafluorophosphate. Potentials were scanned with respect to the quasi-reference electrode in a single compartment cell fitted with Pt electrodes and referenced to the Fc/Fc^+ couple of ferrocene at 0.38 V vs SCE.[43]

EPR Spectroscopy. The X-Band EPR spectrum of **2a** was recorded at ambient temperature on a Bruker EMX-200 spectrometer using a sample of **2a**·MeCN dissolved in degassed toluene. Hyperfine coupling constants were obtained by spectral simulation using Simfonia and WinSim.[44]

Single Crystal Crystallography. For **2a**·MeCN a crystal was mounted on a MiTeGen MicroMount using Fomblin oil, and data were collected at 100 K on a Bruker D8 Venture diffractometer with Mo Kα (λ = 0.71073 Å) radiation collected using Rigaku CrystalClear software[45] and processed with Bruker APEX2 software[46] and SADABS.[47] For **2a**·1/4EtCN a crystal was mounted on a glass fiber and data were collected at 296 K using omega and phi scans with a Bruker kappa APEX II CCD detector and Mo Kα (λ = 0.71073 Å) radiation. Data reduction and structure solution were performed using APEX2 software. During refinement of **2a**·MeCN the presence of channels of residual e-density (possibly disordered MeCN) running parallel to the *a*-axis and located at (x, 1/2, 0) and (x, 0, 1/2) was observed. Analysis of the occupancy of these channels in PLATON suggested the presence of 24 electrons per unit cell. These were excluded from the final refinement using SQUEEZE.[48] An alternative refinement based on a model in which the channels were 1/2-occupied by two disordered carbon atoms afforded R = 0.0510 and R_w = 0.1268, that is, somewhat higher values than those provided in Table 1 for the SQUEEZE model, which is consistent with the results of elemental and thermogravimetric analysis.

Powder Crystallography. High pressure diffraction experiments on **2a**·MeCN were carried out on beamline HMXA at the Canadian Light Source, using synchrotron radiation (λ = 0.509176 Å) and a powdered sample mounted in a diamond anvil cell (DAC), with helium as the pressure transmitting medium. (At room temperature, helium stays in a liquid state up to 14 GPa, hence providing hydrostatic pressure conditions.) A series of data sets was collected over the range 2θ = 1−20° at room temperature and as a function of increasing pressure from 0 to 10.0 GPa. Space group determinations, indexing, and refinement of cell parameters were performed using DASH 3.1.[49] The structures were solved starting from molecular models derived from the ambient pressure crystal structures. During the initial refinement in DASH a rigid-body constraint was maintained. Final Rietveld[50] refinement, using fixed atomic positions and isotropic thermal parameters with an assigned value of 0.025 was performed in GSAS.[51] Atomic positions obtained from DASH were not further refined in GSAS, as a result of which standard deviations for atomic coordinates are not reported in the CIF files.

Magnetic Susceptibility Measurements. DC magnetic susceptibility measurements on **2a**·MeCN and **2a**·1/4EtCN were performed at a field of 1000 Oe over the temperature range 2−300 K on a Quantum Design MPMS SQUID magnetometer. Diamagnetic corrections were made using Pascal's constants.[52]

Ambient Pressure Conductivity Measurements. Four-probe conductivity measurements on cold pressed pellet (1 × 1 × 5 mm) samples of **2a**·MeCN and **2a**·1/4EtCN, and two-probe measurements on single crystals of **2a**·MeCN were performed over the range 200−300 K using home-built equipment (for convenience, the term σ_{RT} refers to the conductivity measured at 298 K). Silver paint (Leitsilber 200) was used to apply the electrical contacts.

Multianvil Press Conductivity Measurements. High pressure conductivity experiments on **2a**·MeCN were performed in a 3000-ton multianvil press using a Cr_2O_3-doped MgO octahedron as the pressure transmitting medium.[53] The pressure was generated by three electric oil pumps, transmitted through a split-cylinder module to six steel wedges, then to eight tungsten carbide (WC) cubes with 32 mm edge length, and finally through the eight truncated corners of these cubes to the octahedral pressure medium. The force-pressure relationships for the 18/11 and 14/8 (octahedral-edge-length (mm)/truncated-edge-length (mm)) cell configurations adopted in these experiments were determined from prior calibrations of the applied hydraulic load against pressures of structure transformations in standards at room temperature (Bi I ↔ II at 2.55 GPa, Bi III ↔ V at 7.7 GPa, Sn I ↔ II at 9.4 GPa, and Pb I ↔ II at 13.4 GPa). A powder sample was densely packed in a boron nitride (σ_{BN} = 10^{-11} S cm^{-1}) cup with Pt disk electrodes in direct contact with the samples at both ends. Four wire AC (Solartron 1260 Impedance Analyzer) resistance measurements were made at a frequency of 1 kHz. A series of resistance measurements was performed at pressures up to 8 GPa at temperatures over the range 223−298 K. Low temperatures were achieved in the multianvil press by selectively and conductively removing heat from the sample volume through six of the eight WC cubes in direct contact with the octahedral pressure cell. Cooling fins made of Cu were sandwiched between, and in thermal contact with, neighboring anvil faces and were each connected to a dedicated Cu heat exchanger chamber through which liquid nitrogen flowed.[54] The contiguous cylinder-shaped sample was extracted from the recovered pressure cell and the sample geometry was measured to convert resistance to conductivity.

Optical Measurements. Polarized reflectance spectra of a single crystal of **2a**·MeCN were measured using a Continuum Thermo-Nicolet FTIR microscope equipped with an MCT detector and integrated with a Nexus-670 FTIR Nicolet spectrometer.

Molecular Electronic Structure Calculations. All DFT calculations on the radical and ionic states of **2a**,**b**,**c** were performed with the Gaussian 09W suite of programs,[55] using the (U)B3LYP hybrid functional and polarized, split-valence basis sets with triple-ζ (6-311G(d,p)) functions. Full geometry optimization was invoked for the calculation of the total SCF energies of each radical, its cation and the various possible states of the anion, that is, closed shell singlet (CSS), triplet (TS) and broken symmetry singlet (BSS). The energy of the open shell singlet (OSS) anion (and hence EA'' and U'') was calculated from the energies of the TS and OSS states, and their respective $\langle S^2\rangle$ expectation values, using the expression $E_{OSS} = E_{TS} - 2[E_{TS} - E_{BSS}]/[\langle S^2\rangle_{TS} - \langle S^2\rangle_{BSS}]$.[56] The Polarized Continuum Model (PCM) with acetonitrile as solvent was invoked to simulate screening effects in solution and the solid state.

Band Electronic Structure Calculations. Band structure calculations on **2a**·MeCN were carried out with the QUANTUM ESPRESSO[57] package using Perdew−Burke−Ernzerhof functionals[58] and ultrasoft pseudopotentials with a plane-wave cutoff of 25 Ry and a 250 Ry integration mesh. Coordinates were taken from the single crystal structures and GSAS refined high pressure powder data. The SCF calculations employed a 4 × 4 × 4 Monkhorst−Pack *k*-point mesh.

■ ASSOCIATED CONTENT

Supporting Information

The Supporting Information is available free of charge on the ACS Publications website at DOI: 10.1021/jacs.6b11779.

Details of powder crystallographic data collection and structure refinement, TGA/DSC and EPR measurements, and DFT calculations (PDF)
Single crystal diffraction data for **2a**·MeCN (CIF)
Single crystal diffraction data for **2a**·1/4EtCN (CIF)
PXRD data for **2a**·MeCN at 2.0 GPa (CIF)
PXRD data for **2a**·MeCN at 4.4 GPa (CIF)
PXRD data for **2a**·MeCN at 6.1 GPa (CIF)

■ AUTHOR INFORMATION

Corresponding Author

*oakley@uwaterloo.ca

ORCID

Richard T. Oakley: 0000-0002-7185-2580

DOI: 10.1021/jacs.6b11779
J. Am. Chem. Soc. 2017, 139, 1625−1635

Notes

The authors declare no competing financial interest.

■ ACKNOWLEDGMENTS

We thank the Natural Sciences and Engineering Research Council of Canada for financial support, the Government of Canada for a Tier I Canada Research Chair to J.S.T. and the Canada Foundation for Innovation for funding a 3000 ton multianvil press. This work is dedicated to the memory of Professor Robert Haddon, a true friend and colleague.

■ REFERENCES

(1) McCoy, N. H.; Moore, W. C. *J. Am. Chem. Soc.* **1911**, *33*, 273.
(2) (a) Haddon, R. C. *Nature* **1975**, *256*, 394. (b) Haddon, R. C. *Aust. J. Chem.* **1975**, *28*, 2333. (c) Haddon, R. C. *Aust. J. Chem.* **1975**, *28*, 2343.
(3) Hubbard, J. *Proc. R. Soc. London, Ser. A* **1963**, *A276*, 238.
(4) This condition assumes a uniform distribution of orbitals in the energy band. A more rigorous treatment of a 1D system affords $W > (\pi/4)\ U$. See: Whangbo, M. H. *J. Chem. Phys.* **1979**, *70*, 4763.
(5) (a) Mott, N. F. *Proc. Phys. Soc., London, Sect. A* **1949**, *62*, 416. (b) Mott, N. F. *Metal-Insulator Transitions*; Taylor and Francis: London, 1990.
(6) (a) Morita, Y.; Suzuki, S.; Sato, K.; Takui, T. *Nat. Chem.* **2011**, *3*, 197. (b) Kubo, T. *Chem. Rec.* **2015**, *15*, 218.
(7) (a) Haddon, R. C.; Wudl, F.; Kaplan, M. L.; Marshall, J. H.; Cais, R. E.; Bramwell, F. B. *J. Am. Chem. Soc.* **1978**, *100*, 7629. (b) Haddon, R. C.; Chichester, S. V.; Stein, S. M.; Marshall, J. H.; Mujsce, A. M. *J. Org. Chem.* **1987**, *52*, 711. (c) Beer, L.; Mandal, S. K.; Reed, R. W.; Oakley, R. T.; Tham, F. S.; Donnadieu, B.; Haddon, R. C. *Cryst. Growth Des.* **2007**, *7*, 802. (d) Goto, K.; Kubo, T.; Yamamoto, K.; Nakasuji, K.; Sato, K.; Shiomi, D.; Takui, T.; Kubota, M.; Kobayashi, T.; Yakusi, K.; Ouyang, J. *J. Am. Chem. Soc.* **1999**, *121*, 1619. (e) Koutentis, P. A.; Chen, Y.; Cao, Y.; Best, T. P.; Itkis, M. E.; Beer, L.; Oakley, R. T.; Cordes, A. W.; Brock, C. P.; Haddon, R. C. *J. Am. Chem. Soc.* **2001**, *123*, 3864.
(8) (a) Kubo, T.; Katada, Y.; Shimizu, A.; Hirao, Y.; Sato, K.; Takui, T.; Uruichi, M.; Yakushi, K.; Haddon, R. C. *J. Am. Chem. Soc.* **2011**, *133*, 14240. (b) Anamimoghadam, O.; Symes, M. D.; Long, D. L.; Sproules, S.; Cronin, L.; Bucher, G. *J. Am. Chem. Soc.* **2015**, *137*, 14944. (c) Huang, J.; Kertesz, M. *J. Am. Chem. Soc.* **2007**, *129*, 1634.
(9) (a) Chi, X.; Itkis, M. E.; Patrick, B. O.; Barclay, T. M.; Reed, R. W.; Oakley, R. T.; Cordes, A. W.; Haddon, R. C. *J. Am. Chem. Soc.* **1999**, *121*, 10395. (b) Huang, J.; Kertesz, M. *J. Am. Chem. Soc.* **2003**, *125*, 13334. (c) Mandal, S. K.; Samanta, S.; Itkis, M. E.; Jensen, D. W.; Reed, R. W.; Oakley, R. T.; Tham, F. S.; Donnadieu, B.; Haddon, R. C. *J. Am. Chem. Soc.* **2006**, *128*, 1982. (d) Pal, S. K.; Itkis, M. E.; Tham, F. S.; Reed, R. W.; Oakley, R. T.; Haddon, R. C. *J. Am. Chem. Soc.* **2008**, *130*, 3942.
(10) (a) Haddon, R. C.; Sarkar, A.; Pal, S. K.; Chi, X.; Itkis, M. E.; Tham, F. S. *J. Am. Chem. Soc.* **2008**, *130*, 13683. (b) Sarkar, A.; Pal, S. K.; Itkis, M. E.; Liao, P.; Tham, F. S.; Donnadieu, B.; Haddon, R. C. *Chem. Mater.* **2009**, *21*, 2226. (c) Bag, P.; Itkis, M. E.; Pal, S. K.; Donnadieu, B.; Tham, F. S.; Park, H.; Schlueter, J. A.; Siegrist, T.; Haddon, R. C. *J. Am. Chem. Soc.* **2010**, *132*, 2684. (d) Bohlin, J.; Hansson, A.; Stafstrom, S. *Phys. Rev. B: Condens. Matter Mater. Phys.* **2006**, *74*, 155111. (e) Bag, P.; Pal, S. K.; Itkis, M. E.; Sarkar, S.; Tham, F. S.; Donnadieu, B.; Haddon, R. C. *J. Am. Chem. Soc.* **2013**, *135*, 12936.
(11) (a) Uchida, K.; Mou, Z.; Kertesz, M.; Kubo, T. *J. Am. Chem. Soc.* **2016**, *138*, 4665. (c) Nishida, S.; Kawai, J.; Moriguchi, M.; Ohba, T.; Haneda, N.; Fukui, K.; Fuyuhiro, A.; Shiomi, D.; Sato, K.; Takui, T.; Nakasuji, K.; Morita, Y. *Chem. - Eur. J.* **2013**, *19*, 11904. (d) Cui, Z. H.; Gupta, A.; Lischka, H.; Kertesz, M. *Phys. Chem. Chem. Phys.* **2015**, *17*, 23963. (e) Kolb, B.; Kertesz, M.; Thonhauser, T. *J. Phys. Chem. A* **2013**, *117*, 3642. (f) Small, D.; Zaitsev, V.; Jung, Y.; Rosokha, S. V.; Head-Gordon, M.; Kochi, J. K. *J. Am. Chem. Soc.* **2004**, *126*, 13850. (g) Beer, L.; Reed, R. W.; Robertson, C. M.; Oakley, R. T.; Tham, F. S.; Haddon, R. C. *Org. Lett.* **2008**, *10*, 3121.
(12) Pal, S. K.; Itkis, M. E.; Tham, F. S.; Reed, R. W.; Oakley, R. T.; Haddon, R. C. *Science* **2005**, *309*, 281.
(13) (a) Cordes, A. W.; Haddon, R. C.; Oakley, R. T. In *The Chemistry of Inorganic Ring Systems*; Steudel, R., Ed.; Elsevier: Amsterdam, 1992; pp 295−321. (b) Oakley, R. T. *Can. J. Chem.* **1993**, *71*, 1775.
(14) (a) Rawson, J. M.; Alberola, A.; Whalley, A. *J. Mater. Chem.* **2006**, *16*, 2560. (b) Hicks, R. G. In *Stable Radicals: Fundamentals and Applied Aspects of Odd-Electron Compounds*; Hicks, R. G., Ed.; John Wiley & Sons, Ltd.: Wiltshire, 2010; pp 317−380. (c) Ratera, I.; Veciana, J. *Chem. Soc. Rev.* **2012**, *41*, 303. (d) Boeré, R. T.; Roemmele, T. L. *Comp. Inorg. Chem. II* **2013**, *1*, 375. (e) Rawson, J. M.; Hayward, J. J. *Handbook of Chalcogen Chemistry: New Perspectives in Sulfur, Selenium and Tellurium*; Devillanova, F., Du Mont, W.-W., Eds.; Royal Society of Chemistry: Cambridge, 2013; Vol 2; pp 69−98. (f) Haddon, R. C. *ChemPhysChem* **2012**, *13*, 3581. (g) Saito, G.; Yoshida, Y. *Bull. Chem. Soc. Jpn.* **2007**, *80*, 1. (h) Saito, G.; Yoshida, Y. *Top. Curr. Chem.* **2011**, *312*, 67.
(15) (a) Bendikov, M.; Wudl, F.; Perepichka, D. F. *Chem. Rev.* **2004**, *104*, 4891. (b) Cortizo-Lacalle, D.; Skabara, P. J.; Westgate, T. D. *Handbook of Chalcogen Chemistry: New Perspectives in Sulfur, Selenium and Tellurium*; Devillanova, F., Du Mont, W.-W., Eds.; Royal Society of Chemistry: Cambridge, 2013; Vol 2; pp 99−126.
(16) (a) Rawson, J. M.; Banister, A. J.; Lavender, I. *Adv. Heterocycl. Chem.* **1995**, *62*, 137. (b) Haynes, D. A. *CrystEngComm* **2011**, *13*, 4793. (c) Melen, R. L.; Less, R. J.; Pask, C. M.; Rawson, J. M. *Inorg. Chem.* **2016**, *55*, 11747.
(17) (a) Cordes, A. W.; Haddon, R. C.; Hicks, R. G.; Oakley, R. T.; Palstra, T. T. M.; Schneemeyer, L. F.; Waszczak, J. V. *J. Am. Chem. Soc.* **1992**, *114*, 1729. (b) Cordes, A. W.; Haddon, R. C.; Oakley, R. T.; Schneemeyer, L. F.; Waszczak, J. V.; Young, K. M.; Zimmerman, N. M. *J. Am. Chem. Soc.* **1991**, *113*, 582. (c) Cordes, A. W.; Haddon, R. C.; Hicks, R. G.; Oakley, R.T.; Palstra, T. T. M.; Schneemeyer, L. F.; Waszczak, J. V. *J. Am. Chem. Soc.* **1992**, *114*, 5000.
(18) (a) Bryan, C. D.; Cordes, A. W.; Haddon, R. C.; Glarum, S. H.; Hicks, R. G.; Kennepohl, D. K.; MacKinnon, C. D.; Oakley, R. T.; Palstra, T. T. M.; Perel, A. S.; Schneemeyer, L. F.; Scott, S. R.; Waszczak, J. V. *J. Am. Chem. Soc.* **1994**, *116*, 1205. (b) Bryan, C. D.; Cordes, A. W.; Fleming, R. M.; George, N. A.; Glarum, S. H.; Haddon, R. C.; MacKinnon, C. D.; Oakley, R. T.; Palstra, T. T. M.; Perel, A. S. *J. Am. Chem. Soc.* **1995**, *117*, 6880. (c) Bryan, C. D.; Cordes, A. W.; Goddard, J. D.; Haddon, R. C.; Hicks, R. G.; MacKinnon, C. D.; Mawhinney, R. C.; Oakley, R. T.; Palstra, T. T. M.; Perel, A. S. *J. Am. Chem. Soc.* **1996**, *118*, 330.
(19) Cordes, A. W.; Haddon, R. C.; Oakley, R. T. *Phosphorus, Sulfur Silicon Relat. Elem.* **2004**, *179*, 673.
(20) (a) Beer, L.; Brusso, J. L.; Cordes, A. W.; Haddon, R. C.; Itkis, M. E.; Kirschbaum, K.; MacGregor, D. S.; Oakley, R. T.; Pinkerton, A. A.; Reed, R. W. *J. Am. Chem. Soc.* **2002**, *124*, 9498. (b) Beer, L.; Britten, J. F.; Brusso, J. L.; Cordes, A. W.; Haddon, R. C.; Itkis, M. E.; MacGregor, D. S.; Oakley, R. T.; Reed, R. W.; Robertson, C. M. *J. Am. Chem. Soc.* **2003**, *125*, 14394. (c) Leitch, A. A.; Reed, R. W.; Robertson, C. M.; Britten, J. F.; Yu, X.; Secco, R. A.; Oakley, R. T. *J. Am. Chem. Soc.* **2007**, *129*, 7903.
(21) (a) Yu, X.; Mailman, A.; Dube, P. A.; Assoud, A.; Oakley, R. T. *Chem. Commun.* **2011**, *47*, 4655. (b) Yu, X.; Mailman, A.; Lekin, K.; Assoud, A.; Dube, P. A.; Oakley, R. T. *Cryst. Growth Des.* **2012**, *12*, 2485. (c) Yu, X.; Mailman, A.; Lekin, K.; Assoud, A.; Robertson, C. M.; Noll, B. C.; Campana, C. F.; Howard, J. A. K.; Dube, P. A.; Oakley, R. T. *J. Am. Chem. Soc.* **2012**, *134*, 2264. (d) Mailman, A.; Winter, S. M.; Yu, X.; Robertson, C. M.; Yong, W.; Tse, J. S.; Secco, R. A.; Liu, Z.; Dube, P. A.; Howard, J. A. K.; Oakley, R. T. *J. Am. Chem. Soc.* **2012**, *134*, 9886. (e) Wong, J. W. L.; Mailman, A.; Winter, S. M.; Robertson, C. M.; Holmberg, R. J.; Murugesu, M.; Dube, P. A.; Oakley, R. T. *Chem. Commun.* **2014**, *50*, 785. (f) Mailman, A.; Winter, S. M.; Wong, J. W. L.; Robertson, C. M.; Assoud, A.; Dube, P. A.; Oakley, R. T. *J. Am. Chem. Soc.* **2015**, *137*, 1044.

DOI: 10.1021/jacs.6b11779
J. Am. Chem. Soc. 2017, 139, 1625−1635

(22) (a) Beneberu, H. Z.; Tianza, Y.-H.; Kertesz, M. *Phys. Chem. Chem. Phys.* **2012**, *14*, 10713. (b) Preuss, K. E. *Polyhedron* **2014**, *79*, 1.
(23) (a) Brusso, J. L.; Derakhshan, S.; Itkis, M. E.; Kleinke, H.; Haddon, R. C.; Oakley, R. T.; Reed, R. W.; Richardson, J. F.; Robertson, C. M.; Thompson, L. K. *Inorg. Chem.* **2006**, *45*, 10958. (b) Brusso, J. L.; Cvrkalj, K.; Leitch, A. A.; Oakley, R. T.; Reed, R. W.; Robertson, C. M. *J. Am. Chem. Soc.* **2006**, *128*, 15080. (c) Leitch, A. A.; Yu, X.; Winter, S. M.; Secco, R. A.; Dube, P. A.; Oakley, R. T. *J. Am. Chem. Soc.* **2009**, *131*, 7112.
(24) Leitch, A. A.; Lekin, K.; Winter, S. M.; Downie, L. E.; Tsuruda, H.; Tse, J. S.; Mito, M.; Desgreniers, S.; Dube, P. A.; Zhang, S.; Liu, Q.; Jin, C.; Ohishi, Y.; Oakley, R. T. *J. Am. Chem. Soc.* **2011**, *133*, 6051.
(25) (a) Robertson, C. M.; Leitch, A. A.; Cvrkalj, K.; Reed, R. W.; Myles, D. J. T.; Dube, P. A.; Oakley, R. T. *J. Am. Chem. Soc.* **2008**, *130*, 8414. (b) Robertson, C. M.; Leitch, A. A.; Cvrkalj, K.; Myles, D. J. T.; Reed, R. W.; Dube, P. A.; Oakley, R. T. *J. Am. Chem. Soc.* **2008**, *130*, 14791. (c) Leitch, A. A.; Brusso, J. L.; Cvrkalj, K.; Reed, R. W.; Robertson, C. M.; Dube, P. A.; Oakley, R. T. *Chem. Commun.* **2007**, 3368.
(26) Winter, S. M.; Hill, S.; Oakley, R. T. *J. Am. Chem. Soc.* **2015**, *137*, 3720.
(27) Wong, J. W. L.; Mailman, A.; Lekin, K.; Winter, S. M.; Yong, W.; Zhao, J.; Garimella, S. V.; Tse, J. S.; Secco, R. A.; Desgreniers, S.; Ohishi, Y.; Borondics, F.; Oakley, R. T. *J. Am. Chem. Soc.* **2014**, *136*, 1070.
(28) Winter, S. M.; Mailman, A.; Oakley, R. T.; Thirunavukkuarasu, K.; Hill, S.; Graf, D. E.; Tozer, S. W.; Tse, J. S.; Mito, M.; Yamaguchi, H. *Phys. Rev. B: Condens. Matter Mater. Phys.* **2014**, *89*, 214403.
(29) Tian, D.; Winter, S. M.; Mailman, A.; Wong, J. W. L.; Yong, W.; Yamaguchi, H.; Jia, Y.; Tse, J. S.; Desgreniers, S.; Secco, R. A.; Julian, S. R.; Jin, C.; Mito, M.; Ohishi, Y.; Oakley, R. T. *J. Am. Chem. Soc.* **2015**, *137*, 14136.
(30) (a) Eugen, K. *German Patent* 3328002-A1 (1985). (b) Sheth, A.; Doshi, N.; Sen, D. J.; Badmanaban, R.; Patel, C. N. *J. Chem. Pharm. Res.* **2010**, *2*, 1.
(31) Tuzun, C.; Oklemer, A.; Yildiz, G.; Birer, S. *Commun. Fac. Sci. Univ. Ankara, Ser. B: Chem. Chem. Eng.* **1988**, *34*, 159.
(32) (a) Herz, R. *Chem. Z.* **1922**, *4*, 948. (b) Warburton, W. K. *Chem. Rev.* **1957**, *57*, 1011.
(33) The cell potential E_{cell} is defined here as the numerical difference between the half-wave potentials for the oxidation and reduction processes, that is, $|E_{cell} = E_{1/2}(ox) - E_{1/2}(red)|$.
(34) Peierls, R. C. *Quantum Theory of Solids*; Oxford University Press: London, 1955; p 108.
(35) (a) Bondi, A. *J. Phys. Chem.* **1964**, *68*, 441. (b) Dance, I. *New J. Chem.* **2003**, *27*, 22.
(36) (a) Williams, J. M.; Ferraro, J. R.; Thorn, R. J.; Carlson, K. D.; Geiser, U.; Wang, H. H.; Kini, A. M.; Whangbo, M.-H. *Organic Superconductors (Including Fullerenes): Synthesis, Structure, Properties and Theory*; Prentice Hall: Englewood Cliffs, NJ, 1992. (b) Mori, T. *Electronic Properties of Organic Conductors*; Springer: Japan, 2016.
(37) (a) Yzambart, G.; Bellec, N.; Ghassan, N.; Jeannin, O.; Roisnel, T.; Fourmigué, M.; Auban-Senzier, P.; Íñiguez, J.; Canadell, E.; Lorcy, D. *J. Am. Chem. Soc.* **2012**, *134*, 17138. (b) Le Gal, Y.; Roisnel, T.; Auban-Senzier, P.; Guizouarn, T.; Lorcy, D. *Inorg. Chem.* **2014**, *53*, 8755.
(38) (a) Jankowski, D.; Świetlik, R.; Jeannin, O.; Assaf, A.; Reinheimer, E. W.; Formigué, M. *J. Raman Spectrosc.* **2013**, *44*, 1765. (b) Ishikawa, T.; Kitayama, M.; Chono, A.; Onda, K.; Okimoto, Y.; Koshihara, S.; Nakano, Y.; Yamochi, H.; Morikawa, T.; Shirahata, T.; Misaki, Y. *J. Phys.: Condens. Matter* **2013**, *24*, 195501. (c) Dressel, M. *ISRN Condens. Matter Phys.* **2012**, *2012*, 732973.
(39) Ioffe, A. F.; Regel, A. R. *Prog. Semicond.* **1960**, *4*, 237.
(40) (a) Schiødt, N. C.; Bjørnholm, T.; Bechgaard, K.; Neumeier, J. J.; Allgeier, C.; Jacobsen, C. S.; Thorup, N. *Phys. Rev. B: Condens. Matter Mater. Phys.* **1996**, *53*, 1773. (b) Belo, D.; Alves, H.; Lopes, E. B.; Duarte, M. T.; Gama, V.; Henriques, R. T.; Almeida, M.; Pérez-Benítez, A.; Rovira, C.; Veciana, J. *Chem. - Eur. J.* **2001**, *7*, 511. (c) Dautel, O. J.; Fourmigué, M.; Canadell, E.; Auban-Senzier, P. *Adv. Funct. Mater.* **2002**, *12*, 693. (d) Tenn, N.; Bellec, N.; Jeannin, O.; Piekara-Sady, L.; Auban-Senzier, P.; Íñiguez, J.; Canadell, E.; Lorcy, D. *J. Am. Chem. Soc.* **2009**, *131*, 16961. (e) Le Pennec, R.; Jeannin, O.; Auban-Senzier, P.; Fourmigué, M. *New J. Chem.* **2016**, *40*, 7113.
(41) Terletska, H.; Vučičević, J.; Tanasković, D.; Dobrosavljević, V. *Phys. Rev. Lett.* **2011**, *107*, 026401.
(42) Chai, C. L. L.; Armarego, W. L. F. *Purification of Laboratory Chemicals*, 5th ed.; Butterworth-Heinemann: New York, 2003.
(43) Boeré, R. T.; Moock, K. H.; Parvez, M. *Z. Anorg. Allg. Chem.* **1994**, *620*, 1589. (b) Boeré, R. T.; Roemmele, T. L. *Coord. Chem. Rev.* **2000**, *210*, 369.
(44) *WinEPR Simfonia*, version 1.25; Bruker Instruments, Inc.: Billerica, MA, 1996.
(45) *CrystalClear*; Rigaku Corporation: Tokyo, Japan, 2005.
(46) *APEX2*; Bruker AXS Inc.: Madison, WI, 2007.
(47) *SADABS*; Bruker AXS Inc.: Madison, WI, 2001.
(48) Spek, A. L. *Acta Crystallogr., Sect. C: Struct. Chem.* **2015**, *71*, 9.
(49) David, W. I. F.; Shankland, K.; van de Streek, J.; Pidcock, E.; Motherwell, W. D. S.; Cole, J. C. *J. Appl. Crystallogr.* **2006**, *39*, 910.
(50) Rietveld, H. M. *J. Appl. Crystallogr.* **1969**, *2*, 65.
(51) Larson, A. C.; Von Dreele, R. B. General Structure Analysis System (GSAS); *Los Alamos National Laboratory Report LAUR 86–748*; 2000.
(52) (a) Carlin, R. L. *Magnetochemistry*; Springer-Verlag: New York, 1986. (b) Bain, G. A.; Berry, J. F. *J. Chem. Educ.* **2008**, *85*, 532.
(53) Secco, R. A.; Yong, W.; Officer, T. New 3000 Ton Multi-Anvil Press at the University of Western Ontario, Abstract MR51A-02, American Geophysical Union Meeting, May 14–17, 2013 Cancun, Mexico.
(54) Secco, R. A.; Yong, W. *Rev. Sci. Instrum.* **2016**, *87*, 123901.
(55) Frisch, M. J.; Trucks, G. W.; Schlegel, H. B.; Scuseria, G. E.; Robb, M. A.; Cheeseman, J. R.; Scalmani, G.; Barone, V.; Mennucci, B.; Petersson, G. A.; Nakatsuji, H.; Caricato, M.; Li, X.; Hratchian, H. P.; Izmaylov, A. F.; Bloino, J.; Zheng, G.; Sonnenberg, J. L.; Hada, M.; Ehara, M.; Toyota, K.; Fukuda, R.; Hasegawa, J.; Ishida, M.; Nakajima, T.; Honda, Y.; Kitao, O.; Nakai, H.; Vreven, T.; Montgomery, Jr., J. A.; Peralta, J. E.; Ogliaro, F.; Bearpark, M.; Heyd, J. J.; Brothers, E.; Kudin, K. N.; Staroverov, V. N.; Kobayashi, R.; Normand, J.; Raghavachari, K.; Rendell, A.; Burant, J. C.; Iyengar, S. S.; Tomasi, J.; Cossi, M.; Rega, N.; Millam, N. J.; Klene, M.; Knox, J. E.; Cross, J. B.; Bakken, V.; Adamo, C.; Jaramillo, J.; Gomperts, R.; Stratmann, R. E.; Yazyev, O.; Austin, A. J.; Cammi, R.; Pomelli, C.; Ochterski, J. W.; Martin, R. W.; Morokuma, K.; Zakrzewski, V. G.; Voth, G. A.; Salvador, P.; Dannenberg, J. J.; Dapprich, S.; Daniels, A. D.; Farkas, O.; Foresman, J. B.; Ortiz, J. V.; Cioslowski, J.; Fox, D. J. *Gaussian 09*, Revision A.02; Gaussian, Inc.: Wallingford, CT, 2009.
(56) (a) Noodleman, L. *J. Chem. Phys.* **1981**, *74*, 5737. (b) Noodleman, L.; Davidson, E. R. *Chem. Phys.* **1986**, *109*, 131. (c) Yamaguchi, K.; Jensen, F.; Dorigo, A.; Houk, K. N. *Chem. Phys. Lett.* **1988**, *149*, 537. (d) Nagao, H.; Nishino, M.; Shigeta, Y.; Soda, T.; Kitagawa, Y.; Onishi, T.; Yoshika, Y.; Yamaguchi, K. *Coord. Chem. Rev.* **2000**, *198*, 265.
(57) Giannozzi, P.; Baroni, S.; Bonini, N.; Calandra, M.; Car, R.; Cavazzoni, C.; Ceresoli, D.; Chiarotti, G. L.; Cococcioni, M.; Dabo, I.; Dal Corso, A.; Fabris, S.; Fratesi, G.; de Gironcoli, S.; Gebauer, R.; Gerstmann, U.; Gougoussis, C.; Kokalj, A.; Lazzeri, M.; Martin-Samos, L.; Marzari, N.; Mauri, F.; Mazzarello, R.; Paolini, S.; Pasquarello, A.; Paulatto, L.; Sbraccia, C.; Scandolo, S.; Sclauzero, G.; Seitsonen, A. P.; Smogunov, A.; Umari, P.; Wentzcovitch, R. M. *J. Phys.: Condens. Matter* **2009**, *21*, 395502.
(58) (a) Perdew, J. P.; Burke, K.; Ernzerhof, M. *Phys. Rev. Lett.* **1996**, *77*, 3865. (b) Perdew, J. P.; Burke, K.; Ernzerhof, M. *Phys. Rev. Lett.* **1997**, *78*, 1396.

DOI: 10.1021/jacs.6b11779
J. Am. Chem. Soc. 2017, 139, 1625–1635